



Cite this: *RSC Adv.*, 2017, 7, 24754

Highly efficient visible-light photocatalytic activity of MoS₂–TiO₂ mixtures hybrid photocatalyst and functional properties†

M. Sabarinathan,^{ab} S. Harish,^{ab} J. Archana,^c M. Navaneethan,^{id}*^b H. Ikeda^b and Y. Hayakawa^{id}*^{ab}

2-D-layered molybdenum disulfide (MoS₂) and MoS₂/TiO₂ nanocomposite were synthesized by a hydrothermal method. The effects of the concentration of TiO₂ on the formation of MoS₂/TiO₂ composites and functional properties were investigated. X-ray diffraction patterns revealed the formation of hexagonal and anatase structure of MoS₂ and TiO₂, respectively. Core-level X-ray photoelectron spectroscopy confirmed the presence of Mo and Ti interaction by a significant peak shift. Morphological analysis revealed the formation of TiO₂ on the surface of the MoS₂ nanosheets. The photocatalytic degradation of methylene blue (MB) in an aqueous suspension was employed to evaluate the visible-light activity of the as-prepared composite photocatalyst. The MB absorption peaks completely disappeared after 12 min with 99.33% of degradation under visible-light irradiation at the TiO₂ concentration of 0.005 M. It was found that hydroxyl radical ([•]OH) played an important role in the degradation of MB under visible-light irradiation. The possible charge-transfer mechanism has been proposed in this study.

Received 29th March 2017

Accepted 20th April 2017

DOI: 10.1039/c7ra03633g

rsc.li/rsc-advances

1. Introduction

Energy crisis and environmental remediation are the two most important issues that need to be resolved for living beings and the society. The sun irradiates 1.5×10^{18} kW h energy to earth every year, which is approximately 28 000 times of the total annual energy consumption.¹ Hence, semiconductor photocatalysis seems to be more attractive and easier to apply for clean energy production and environmental remediation.^{2–4} The photocatalytic activities of a semiconductive material depend on several factors such as absorption ability of photocatalysts, separation and transport rate of the photogenerated electrons and holes, and photoabsorption ability in the available light energy region. Titanium dioxide (TiO₂) is one of the most explored and traditional semiconductor photocatalysts.⁵ It has a strong oxidizing power, high stability, low-cost, an abundant source, and is relatively non-toxic.^{6–10} However, TiO₂ responds only to UV light, which is only 3–5% of the total sunlight.¹¹ The

band gap of TiO₂ is 3.0 and 3.2 eV for the rutile and anatase phases, respectively, which is not compatible with visible-light excitation.¹² Since the electron–hole recombination rate is faster, it is mainly responsible for its limited application in catalysis.¹³ Therefore, it is necessary to overcome this drawback by charge separation *via* suppressing the recombination rate of the electron and hole pairs.

MoS₂ has drawn extensive attention because of its layered structure, similar to that of graphene. Each layer is composed of three atomic layers stacked together, in which Mo atom in the middle is strongly bonded to S atoms present above and below.^{14,15} This two-dimensional (2D)-layered crystal structure provides convenient electron transfer and many active sites for sunlight absorption. The band gap of MoS₂ increases with the decreasing number of layers due to quantum confinement effect. The direct band gap of ~ 1.8 eV makes it a visible-light active photocatalyst.^{16,17} The advantages of MoS₂ include strong oxidizing activity, high hardness, high stability and reliability, low-cost, and non-toxicity.^{18–23} Researchers have focused on synthesizing heterostructure nanocomposites such as MoS₂/RGO, MoS₂/TiO₂, MoS₂/CuO, MoS₂/CuS, and MoS₂/MoO₃.^{24–29} Among these, MoS₂/TiO₂ heterostructure is the best photocatalyst under visible-light irradiation due to the separation of charge carriers. MoS₂/TiO₂ nanostructures possess more surface-active sites than other nanostructures and this enhances the light absorption by the photocatalysts.^{30,31} Recently, Z. B. Chen and his co-workers have prepared MoO₃–MoS₂ core–shell nanostructures by chemical vapor deposition method and studied the photocatalytic hydrogen evolution

^aGraduate School of Science and Technology, Research Institute of Electronics, Shizuoka University, 3-5-1 Johoku, Naka-ku, Hamamatsu, Shizuoka 432-8011, Japan. E-mail: hayakawa.yasuhiro@shizuoka.ac.jp; Fax: +81 53 4781338; Tel: +81 53 4781338

^bResearch Institute of Electronics, Research Institute of Electronics, Shizuoka University, 3-5-1 Johoku, Naka-ku, Hamamatsu, Shizuoka 432-8011, Japan. E-mail: mpnavaneethan@yahoo.co.in

^cSRM Research Institute, Department of Physics and Nanotechnology, SRM University, Kattankulathur, Chennai, 603203, Tamilnadu, India

† Electronic supplementary information (ESI) available. See DOI: 10.1039/c7ra03633g



reaction.³² B. Pourabbas *et al.* have synthesized MoS₂ photocatalysts by hydrothermal method at 300 °C and 12 h and investigated the photooxidation of phenol.³³ X. Zu and co-workers have synthesized TiO₂-decorated MoS₂ nanosheets by hydrothermal method at 220 °C and 24 h.³⁴ L. Cao *et al.* have synthesized MoS₂-hybridized TiO₂ nanosheets by hydrothermal growth at 210 °C for 24 h and measured its visible light photocatalytic activity.³⁵ R. Tang *et al.* have demonstrated a facile two-step hydrothermal method (200 °C for 24 h) to synthesize layered MoS₂-coupled metal-organic framework (MOF)-derived dual-phase TiO₂ (MDT) as photoanodes for photoelectrochemical water splitting and dye-sensitized solar cells (DSSCs).³⁶ H. Li *et al.* have synthesized layered MoS₂ nanosheet-coated TiO₂ nanobelts by hydrothermal method at 200 °C and 24 h.³⁷ Meng Shen *et al.* have prepared MoS₂ nanosheet/TiO₂ nanowire hybrid nanostructures by a hydrothermal method at 240 °C and 24 h and studied their visible-light photocatalytic activities.³⁸ However, these reports are related to high-temperature synthesis; therefore, relatively low temperature (<200 °C) synthesis of MoS₂/TiO₂ nanocomposites is limited because of poor crystallinity and non-uniform distribution in the morphology. Therefore, a new approach has to be developed to realize the mass production of MoS₂ at relatively low temperature (*i.e.* <200 °C). X. Zong *et al.* have synthesized CdS/MoS₂ heterostructure photocatalyst using a hot-wire chemical vapor deposition method (HWCVD), and they found that the H₂ production enhanced under visible-light irradiation.³⁹ Weijia Zhou *et al.* have synthesized few layers of 2-D MoS₂/TiO₂ composite photocatalyst by a hydrothermal method at 200 °C and 24 h, and they found that the light absorption range for the photocatalytic H₂ production was enhanced.⁴⁰ As is well-known, coupling of two semiconductors with narrow and wide band gaps could extend the solar spectrum for light utilization. Therefore, it is necessary to couple two semiconductors with matched energy levels to enhance the photocatalytic activity under visible-light irradiation through interfacial charge transfer between MoS₂ and TiO₂ nanosheets.⁴¹

Herein, the layered MoS₂ and MoS₂/TiO₂ nanosheets were synthesized by a hydrothermal method. The effects of TiO₂ concentration on the formation of the nanosheets were investigated. The photocatalytic activity of the synthesized materials was characterized by quantifying the rate of methylene blue (MB) degradation in an aqueous suspension under visible-light irradiation. MoS₂/TiO₂ nanocomposite photocatalyst exhibited enhanced light absorption capacity as compared to pure MoS₂ and TiO₂ photocatalysts. Kinetics, electron trapping, and possible photocatalytic mechanism were studied.

2. Experimental

Sodium molybdate dihydrate [(Na₂MoO₄·2H₂O), 99.5%], thioacetamide [(C₂H₅NS), 98%], citric acid [(C₆H₈O₇), 98%], and diammonium hexafluorotitanate (DAHFT) [(NH₄)₂TiF₆], 95% were purchased from Wako chemicals (Japan) and used without further purification.

2.1 Synthesis of 2D-layered MoS₂ nanostructures

2D-layered MoS₂ nanosheets were prepared by a hydrothermal method similar to a previous report.⁴² In a typical synthesis, 0.04 M of sodium molybdate dihydrate, 0.08 M of thioacetamide, and 0.04 M of citric acid were dissolved in 50 mL of deionized water under vigorous stirring for 4 h. The transparent aqueous solution was transferred into a 100 mL stainless steel autoclave and maintained at 180 °C for 24 h. The final product was obtained from the autoclave through centrifuging thrice with deionized water and ethanol and drying at 80 °C for 10 h. The sample was labelled as S1.

2.2 Synthesis of layered MoS₂-TiO₂ mixture heterostructure

The MoS₂-TiO₂ mixture heterostructures were prepared by a hydrothermal method. The amount of DAHFT, as a Ti source, was changed as a parameter. In a typical reaction process, 0.04 M of sodium molybdate dihydrate, 0.08 M of thioacetamide, (0.0015, 0.0030, 0.0050, 0.010, and 0.015 M) of DAHFT, and 0.04 M of citric acid were dissolved in 50 mL deionized water under vigorous stirring for 4 h. The transparent aqueous solution was transferred into a 100 mL stainless steel autoclave and maintained at 180 °C for 24 h. The final product was obtained from the autoclave and centrifuged thrice with deionized water and ethanol and dried at 80 °C for 10 h. The samples were labelled as S2 (0.0015 M), S3 (0.0030 M), S4 (0.0050 M), S5 (0.010 M), and S6 (0.015 M).

2.3 Photocatalytic dye degradation

Photocatalytic degradation of methylene blue (MB) was carried out under visible-light irradiation. The optical absorption of MB at 664 nm was used as a monitor wavelength of photodegradation. Then, 5 mg of MB was added to 100 mL of aqueous solution and stirred for 30 min. After this, 50 mg of MoS₂ and MoS₂/TiO₂ photocatalysts were separately added to the above-mentioned solution. To establish absorption/desorption equilibrium, the mixed solution was stirred for 30 min in the dark before the photodegradation reaction. The xenon lamp as a visible light source was placed 15 cm away from the surface of the solution. The dye degradation surveys were conducted at the interval of 4 min, and the catalyst was isolated *via* centrifugation. The photodegradation percentage of MB was calculated using the following equation:⁴³

$$D(\%) = \frac{C_0 - C_t}{C_0} \times 100 \quad (1)$$

where C_0 and C_t are the concentrations of MB at time 0 and t (s), respectively, and t is the irradiation time.

2.4 Characterization

The structure of the product was characterized by powder X-ray diffraction (XRD) using a Rigaku diffractometer (RINT ULTIMA - 2200, Japan, Cu K α radiation). X-ray photoelectron spectroscopy (XPS) was performed *via* a Kratos analytical instrument (Shimadzu Corporation, ESCA 3400, Japan). Surface morphologies were characterized by field-emission scanning



electron microscopy (FESEM) using a JEOL JSM 7001F microscope at an accelerating voltage of 15 kV. Transmission electron microscopy (TEM) images were obtained using a JEOL JEM 2100F microscope at an accelerating voltage of 200 kV. UV-visible spectroscopy (JASCO V - 670) was used to detect the absorbance of the MB dye degradation.

3. Results and discussion

Fig. 1 shows the powder XRD patterns of pure MoS₂ and MoS₂/TiO₂ nanocomposites. Fig. 1 (S1) shows pure MoS₂ with its diffraction peaks. The peaks corresponded to the hexagonal phase of MoS₂, which matched well with the standard JCPDS card number (024-0513). Peaks at 14.4°, 32.6°, 35.8°, 44.2°, and 58.2° can be indexed to the (002), (100), (102), (104), and (110) crystal planes, respectively. After the addition of TiO₂, new peaks appeared at 25.2°, 37.8°, 48.0°, 53.8°, 55.0°, and 62.6°, which corresponded to the (101), (103), (200), (105), (211), and (204) crystal planes, respectively. This confirmed the presence of TiO₂ in the nanocomposites. As the concentration of TiO₂ increased, the peak intensity of TiO₂ also increased. The structures of MoS₂ and TiO₂ in all the samples were indexed to the hexagonal (024-0513) and anatase structure (021-1272), respectively. No other characteristic peaks were observed.

XPS measurement was carried out to observe the chemical state of the MoS₂ and MoS₂/TiO₂ nanocomposite. Fig. 2 shows the survey spectra of MoS₂/TiO₂. The characteristic peaks at 36.90, 161.80, 229.40, and 529.89 eV can be attributed to Ti 3p, S 2p, Mo 3d, and O 1s, respectively. The high resolution XPS spectra of Ti 3p, S 2p, Mo 3d, and O 1s are shown in Fig. 3. Herein, two symmetric peaks appeared for Mo 3d state, as shown in Fig. 3(a1–a6). The peaks centered at 228.30 and 231.45 eV (S1) can be attributed to the Mo 3d_{5/2} and Mo 3d_{3/2} states, respectively, indicating a +4 oxidation state.⁴⁴ The energy separation between the Mo 3d_{5/2} and Mo 3d_{3/2} states was 3.1 eV, which was in good agreement with the standard value.⁴⁵ The binding energies of the sample S2 were shifted to 227.80 and 231 eV from 228.30 and 231.45 eV of pure MoS₂, respectively. On

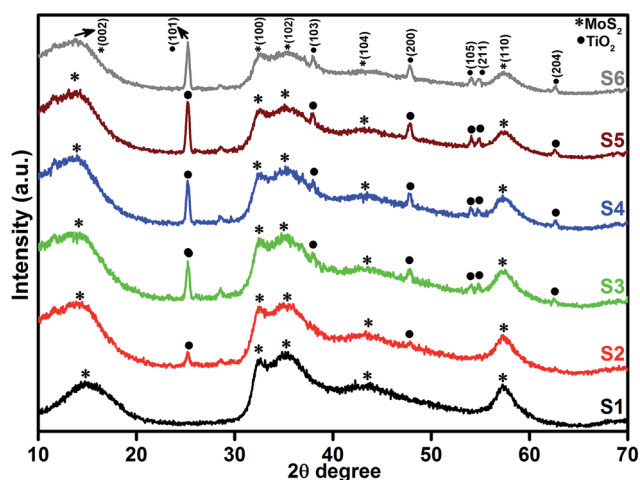


Fig. 1 XRD patterns of the layered MoS₂ and TiO₂ nanosheets.

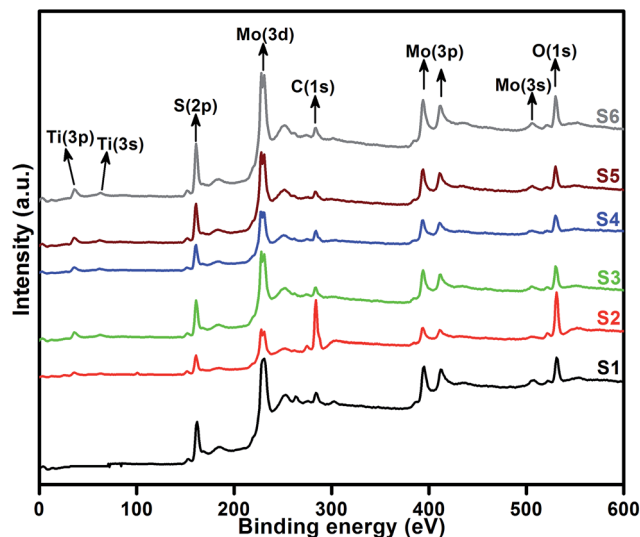


Fig. 2 High resolution XPS spectra of the layered MoS₂ and TiO₂ nanosheets.

further increasing the concentration of TiO₂, the peaks shifted to 227.90 and 231 eV for the sample S3, 227.55 and 230.80 eV for the sample S4, 227.55 and 230.80 eV for the sample S5, and 227.5 and 230.80 eV for the sample S6. The samples showed significant peak shift because of strong interaction between Mo and Ti. The S 2p spectra, as shown in Fig. 3(b1–b6), can be deconvoluted into two peaks located at 161 and 162.05 eV, which can be attributed to the S 2p_{3/2} and S 2p_{1/2} orbitals of divalent sulfide ions (S²⁻). The energy separation between S 2p_{3/2} and S 2p_{1/2} was 1.1 eV, which was in good agreement with the reported value.⁴⁶ The binding energies shifted to 160.50 and 161.72 for the sample S2, 160.75 and 161.95 for the sample S3, 160.52 and 161.70 for the sample S4, and 160.52 and 161.70 for the sample S5. Moreover, for the samples S4 (a4, b4), S5 (a5, b5), and S6 (a6, b6), binding energies of Mo 3d_{5/2}, Mo 3d_{3/2}, S 2p_{3/2}, and S 2p_{1/2} were shifted about 0.20 eV when compared with those of the samples S2 (a2) and S3 (a3). This slight shift was attributed to the strong interaction between MoS₂ and TiO₂. Fig. 3(c1–c5) shows the Ti 3p state with the peak centered at 37 eV. There was no significant peak shift observed in the Ti 3p state. O 1s states of the samples are shown in Fig. 3(d1–d5). All the samples exhibited an asymmetrical shape and two symmetrical peaks centered at 530.85 eV and 532.50 eV, indicating two different types of O species in the samples. The binding energy of 530.85 eV corresponded to O²⁻ ions surrounded by Ti in the TiO₂ compound system. The shoulder peak observed at 532.50 eV corresponded to the chemisorbed oxygen, dissociated oxygen, or OH⁻ groups on the surface. Similar shift in the peaks was observed as the concentration of TiO₂ was increased, 530.60 eV for sample S3, 530 eV for sample S4, 530 eV for sample S5, and 530 eV for sample S6. O 1s binding energy of the abovementioned samples was shifted about 0.20 eV when compared with those of the samples S1 (d1) and S2 (d2). The XPS measurement confirmed the presence of TiO₂ in the prepared nanocomposites.

The morphological analysis was performed using FESEM, TEM, and HRTEM, as shown in Fig. 4. Fig. 4(a) shows the monodispersed pure MoS₂ (S1) nanosheets with a layered structure.



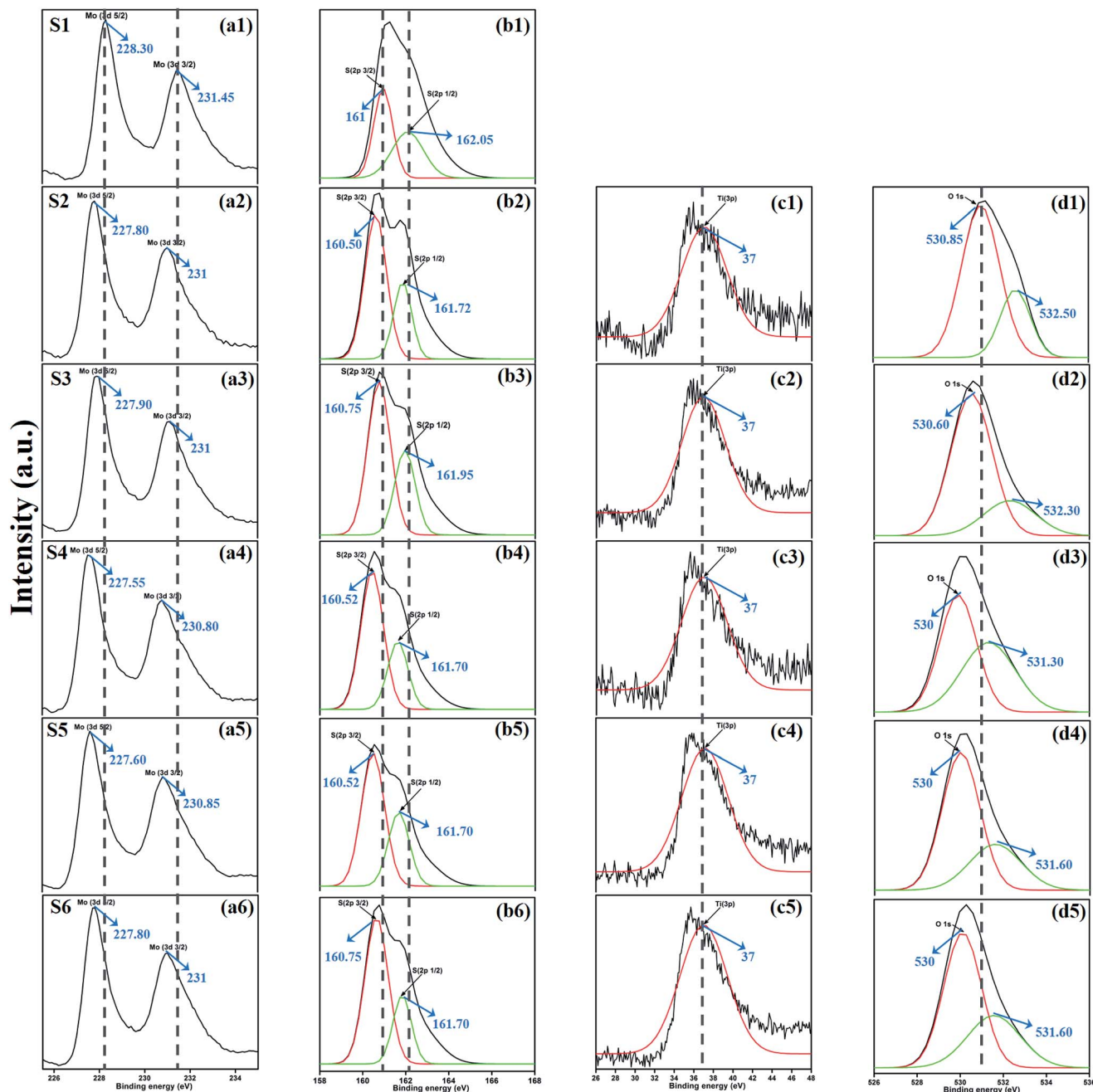


Fig. 3 XPS spectra of the Mo 3d state (a1–a6), S 2p state (b1–b6), Ti 3p state (c1–c5), and O 1s state (d1–d5) of samples S1 to S6.

The thickness of each layer was about 20–50 nm. When TiO_2 was incorporated into the MoS_2 nanosheets, TiO_2 agglomerated on the surface of the nanosheets. This was evident from the FESEM images of S4 (j), S5 (m), and S6 (p). This agglomeration was attributed to the increased ionic strength of the TiO_2 nanoparticles. The layered structure of the sample was further characterized by TEM and HRTEM, as shown in Fig. 4(b) and (c). MoS_2 nanosheets had 5–9 layers and the lattice d -spacing was 0.61 nm, which corresponded to the (002) plane. Fig. 4(d)–(f) show the FESEM, TEM, and HRTEM images of the $\text{MoS}_2/\text{TiO}_2$ nanocomposites of the S2 sample, respectively. In the HRTEM images (f, i, l, o, and r), white dashed line corresponded to the MoS_2 -

layered nanosheets and white squared dot line indicated the TiO_2 nanosheets. When the concentration of TiO_2 was increased from 0.0015 to 0.015 M, formation of TiO_2 nanosheets was observed in the samples S2 to S6. Nanocomposites were composed of MoS_2 and TiO_2 , as shown in Fig. 4. It can be concluded from XPS and TEM analysis that the layered MoS_2 nanosheets and TiO_2 were formed as composites.

3.1 Photocatalytic activity

Photocatalytic performances of MoS_2 and $\text{MoS}_2/\text{TiO}_2$ photocatalyst were examined by degrading MB under visible-light



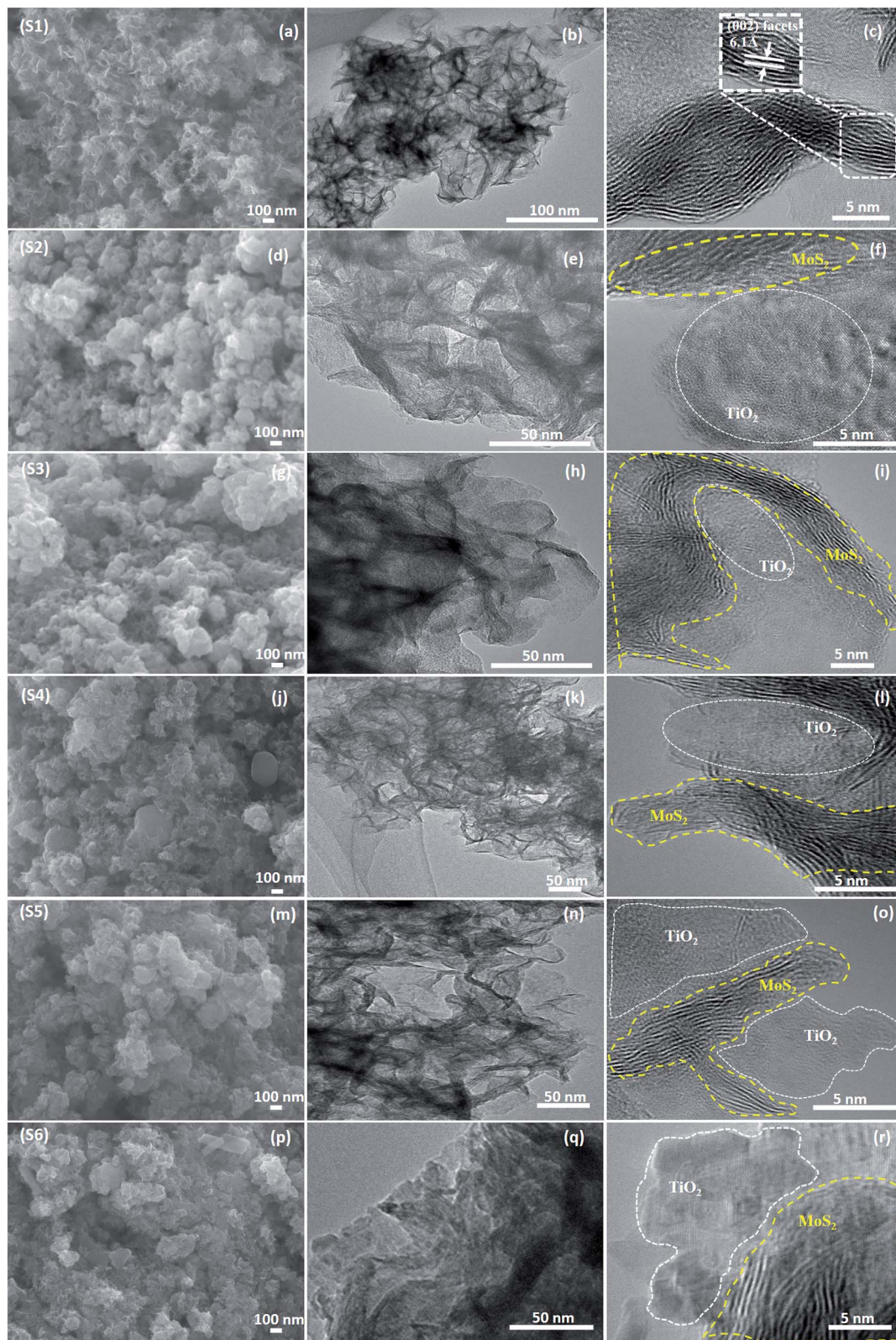


Fig. 4 (a, d, g, j, m, and p) FESEM, (b, e, h, k, n, and q) TEM and (c, f, i, l, o, and r) HRTEM images of the samples S1 to S6.

irradiation. The characteristic absorption peak of MB at 664 nm was chosen to monitor the photocatalytic degradation of MB. Fig. 5 shows the time-dependent absorption spectra of pure

MoS₂ (S1) and MoS₂/TiO₂ (S2–S6). The intensity of the absorption peak at 664 nm rapidly decreased with illumination time and the peak almost disappeared after 32 min for sample S1.



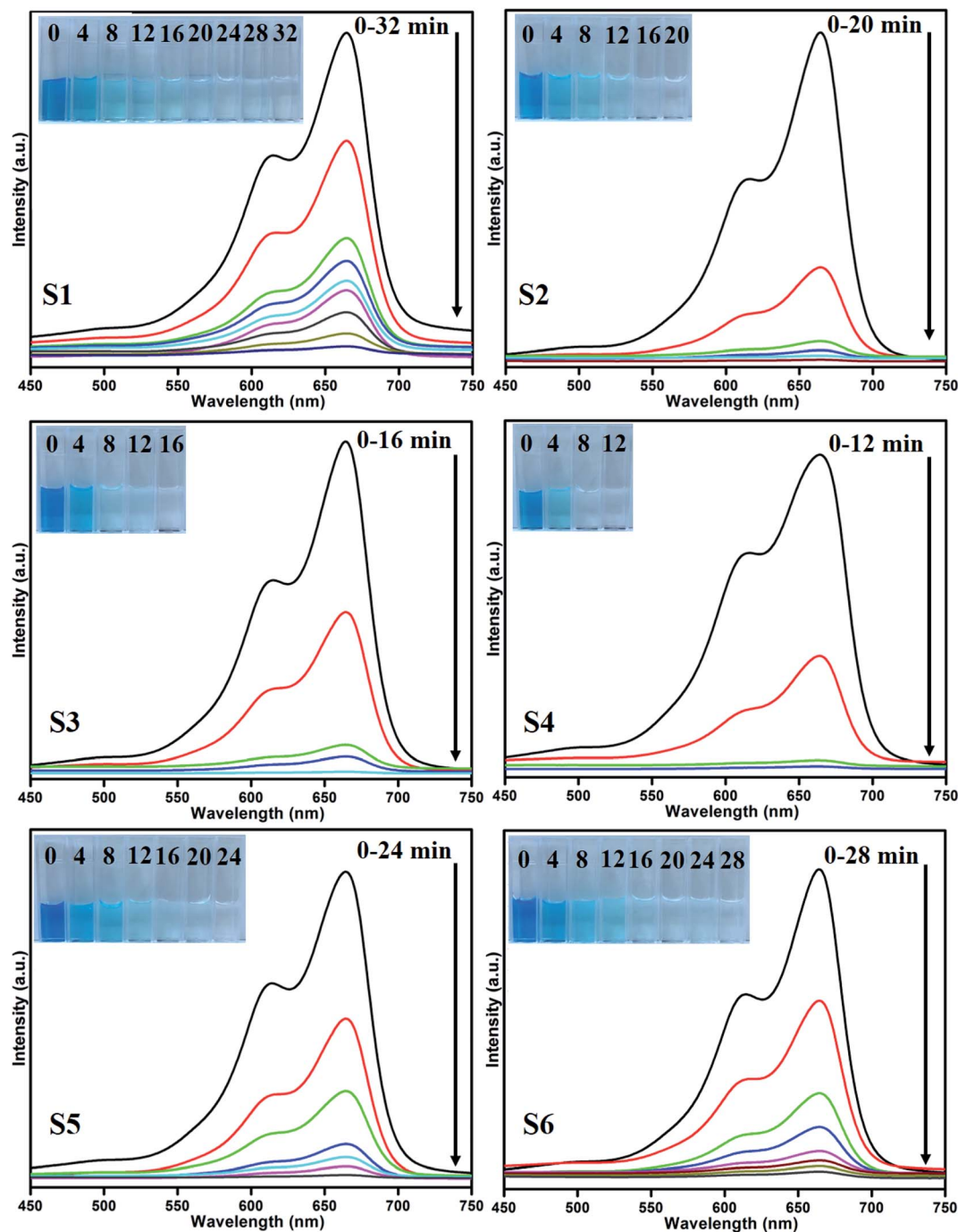


Fig. 5 UV absorbance spectra of the MB samples S1 (a), S2 (b), S3 (c), S4 (d), S5 (e), and S6 (f).

However, for S2, S3, S4, S5, and S6 samples, irradiation time was decreased to 20, 16, 12, 24, and 28 min, respectively. Fig. 6 shows that the percentage of degradation for the samples S1, S2, S3, S4, S5, S6, and P25 (TiO_2) is 99.20, 99.17, 98.68, 99.33, 98.08, 98.90, and 56.89%, respectively. Moreover, 71.50, 93.99, 96.79, 99.17, 88.25, and 84.21% MB was degraded in 12 min of irradiation for sample S1, S2, S3, S4, S5, and S6, respectively. It was evident that the photodegradation efficiency of the $\text{MoS}_2/\text{TiO}_2$ photocatalyst was significantly higher than that of pure MoS_2 and TiO_2 (P25). Among all the synthesized samples, S4 showed

enhanced photocatalytic activity because the oxidation state of $\text{MoS}_2/\text{TiO}_2$ photocatalyst provided more surface-active sites and strong absorption ability towards organic dye molecules. Moreover, the layered nanosheets favored the photogenerated charge carrier transfer from TiO_2 to MoS_2 . It is a key factor in determining the photocatalytic activities of layered $\text{MoS}_2/\text{TiO}_2$ nanocomposites as a photocatalyst. The formation of synergetic interaction between the MoS_2 and TiO_2 semiconductors provided an efficient transport platform for charge carrier transfer and enhanced the photocatalytic activities.



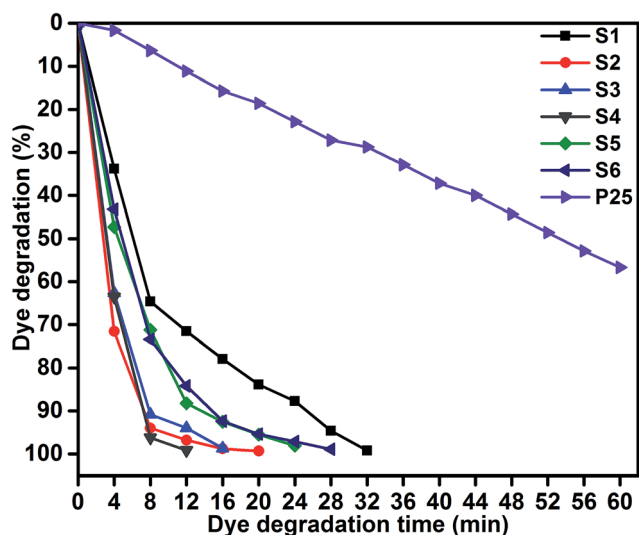


Fig. 6 MB degradation of samples S1, S2, S3, S4, S5, S6, and P25: time (min) vs. dye degradation (%).

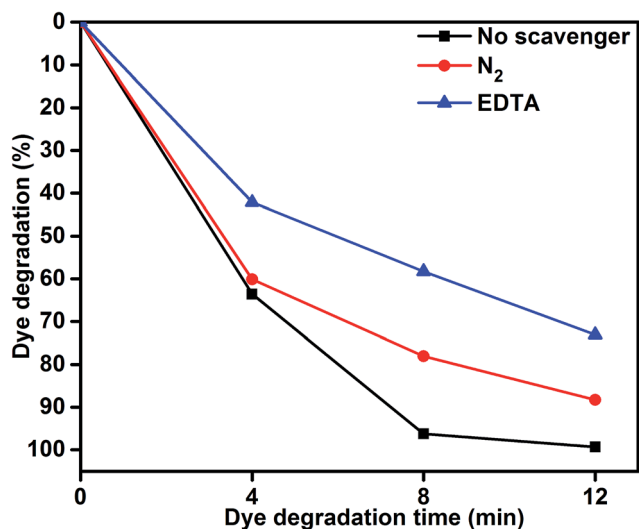


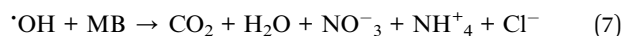
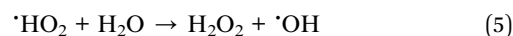
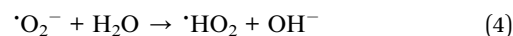
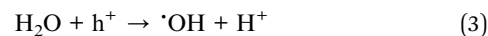
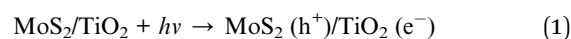
Fig. 7 MB degradation using the MoS₂/TiO₂ nanosheets without scavenger and with scavengers under visible-light irradiation.

To understand the role of photocatalytic activity, free radical trapping experiments were carried out, as shown in Fig. 7. In general, during photocatalysis, hydroxyl radicals ($\cdot\text{OH}$) and superoxide anions ($\text{O}_2^{\cdot-}$) are the possible reactive species for the degradation of organic pollutants. Disodium ethylenediaminetetraacetate (EDTA-2Na) and N_2 were used as a hole (h^+) and electron acceptor scavenger, respectively.^{47,48} A high purity N_2 gas was continuously purged throughout the reaction process under ambient conditions, which eliminated the dissolved oxygen from the reaction solution and thereby prevented the formation of $\text{O}_2^{\cdot-}$. The degradation percentage of MB was 88.39% after 12 min irradiation as compared 99.33% in the scavenger-free photocatalyst. This conformed that superoxide anions played a minor role in the photocatalytic degradation of organic pollutants. To further determine the degradation mechanism, EDTA was added

into the solution as a $\cdot\text{OH}$ radical scavenger. The dye degradation was 72.90%, which indicated suppression of the MB degradation rate. This result confirmed that the photoinduced holes (h^+) were one of the main reactive species for the degradation of MB. Therefore, these results clearly determined that MB degradation mainly depended on the photogenerated $\cdot\text{OH}$ radical. The possible reason for dye degradation by MoS₂/TiO₂ as a photocatalyst was that superoxide anion radical had the potential to directly react *via* oxidative pathways. It can also produce singlet oxygen or decompose to H_2O_2 , and transform to hydroxyl radical during MoS₂/TiO₂ photocatalysis process.^{49–51} This process was explained in the dye degradation mechanism of MB under visible-light irradiation. These results suggested that the rate of photocatalytic degradation of MB was suppressed in the presence of EDTA as a hole (h^+) scavenger. Moreover, the reactive species of superoxide anions ($\text{O}_2^{\cdot-}$) played a minor role in the degradation of MB. The obtained results indicated that the rate of photocatalytic degradation not only depended on organics but also on the nature of the catalysts.

Fig. 8 shows the kinetic plot of $\ln(C_0/C_t)$ versus irradiation time to investigate whether the process obeyed pseudo-first-order model. A linear correlation existed between $\ln(C_0/C_t)$ versus irradiation time. The kinetic data was obtained by the pseudo-first order model. The apparent rate constants (K_{app}), corresponding correlation coefficients (R^2), and maximum dye degradation in presence of MoS₂ and MoS₂/TiO₂ nanocomposites are presented in Table 1. The apparent rate constant K_{app} was 0.0965, 0.2512, 0.2895, 0.4162, 0.162, and 0.1564 min^{-1} for S1, S2, S3, S4, S5, and S6, respectively. K value increased with the increase in the concentration of TiO₂ from 0.0965 to 0.4162 min^{-1} for the samples S1 to S4. With further increase in the TiO₂ concentration, K value decreased to 0.1564 min^{-1} for sample S6. Plots of $\ln(C_0/C_t)$ versus irradiation time show that apparent rate constant was about two times higher for MoS₂/TiO₂ nanocomposites than that for pure MoS₂. A comparison was carried out between the photocatalytic performance of the materials developed in this study and those of other recently reported MoS₂/TiO₂ composite nanostructures, as shown in Table 2.

Based on the abovementioned results, we proposed the possible photocatalytic mechanism for the degradation of MB using MoS₂/TiO₂ as photocatalysts:⁵²



As shown in Fig. 9, the reusability of the sample S4 photocatalyst for the degradation of methylene blue was studied over



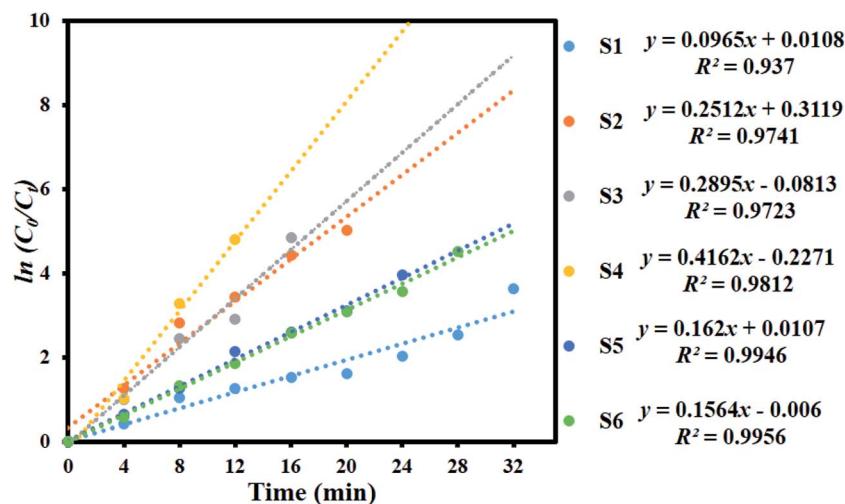


Fig. 8 Kinetic plot of $\ln(C_0/C_t)$ as a function of time (min) for the degradation of MB.

Table 1 Observed pseudo-first-order rate constants, R^2 values, maximum degradation (%), and time required for maximum degradation by the $\text{MoS}_2/\text{TiO}_2$ nanosheets

Sample code	K_{app} ($\text{MoS}_2/\text{TiO}_2$)	R^2	Maximum degradation (%)	Time taken for maximum degradation (min)
S1	0.0965	0.937	99.17	32
S2	0.2512	0.9741	99.10	20
S3	0.2895	0.9723	98.68	16
S4	0.4162	0.9812	99.33	12
S5	0.162	0.9946	98.08	24
S6	0.1564	0.9956	98.90	28

Table 2 Comparison of the photocatalytic performances of the $\text{MoS}_2/\text{TiO}_2$ composites in this research with that of those reported in literatures

Material	Light source	Dye	Dye degradation (%)	Time taken for degradation (min)	Ref.
$\text{MoS}_2/\text{TiO}_2$	500 W xenon lamp	RhB	81.8	180	40
$\text{MoS}_2/\text{TiO}_2$	30 W day lamp	MB	98	90	55
$\text{MoS}_2/\text{TiO}_2$	30 W day lamp	MO	95.1	120	56
$\text{MoS}_2/\text{TiO}_2$	500 W xenon lamp	MO	97	60	57
$\text{MoS}_2/\text{TiO}_2$	300 W xenon lamp	RhB	86.9	20	58
$\text{MoS}_2/\text{TiO}_2$	400 W Asahi spectra(xenon lamp)	MB	99.33	12	This work

four cycles under visible-light irradiation. The dye concentration was adjusted each time to its initial value. Photocatalysts were reused for four cycles and the obtained degradation values were 95.18, 92.80, 86.66, and 83.15. The efficiency of the sample S4 did not significantly decline, which suggested that the catalyst had good stability and sustainability. (Fig. S1, ESI†) shows the XRD patterns of the sample S4 after five runs. It can be clearly seen that the phase and structure of the sample S4 remained the same. In addition, the chemical state of Mo 3d, S 2p, Ti 3p, and O 1s were investigated by XPS spectra, as shown in (Fig. S2, ESI†). It suggested that the binding energies of Mo, S, Ti, and O showed no peak shift after four cycles as compared to those of the as-prepared sample.

The schematic (Fig. 10) illustrates the energy band structure and charge transfer mechanism. MoS_2 is a narrow band

gap (1.9 eV) semiconductor with a work function of 4.52 eV, whereas anatase TiO_2 is a wide band gap (3.2 eV) semiconductor with a work function of 4.5 eV.^{19,53,54} Under visible-light irradiation, electrons are excited from the valance band of MoS_2 to the conduction band, leaving behind holes in the valance band. The photoinduced electrons in the conduction band of MoS_2 were transferred to the conduction band of TiO_2 , which acted as a photoelectronic receiver. The photogenerated holes reacted with either water (H_2O) or hydroxyl ions (OH^-) adsorbed onto the catalyst surface to produce hydroxyl radicals ($\cdot\text{OH}$), and the photogenerated electrons reacted with oxygen (O_2) to form superoxide radicals ($\cdot\text{O}_2^-$). Consequently, both $\cdot\text{OH}$ and $\cdot\text{O}_2^-$ radicals can decompose the organic compounds to form CO_2 , H_2O , and other inorganic molecules as harmless compounds.



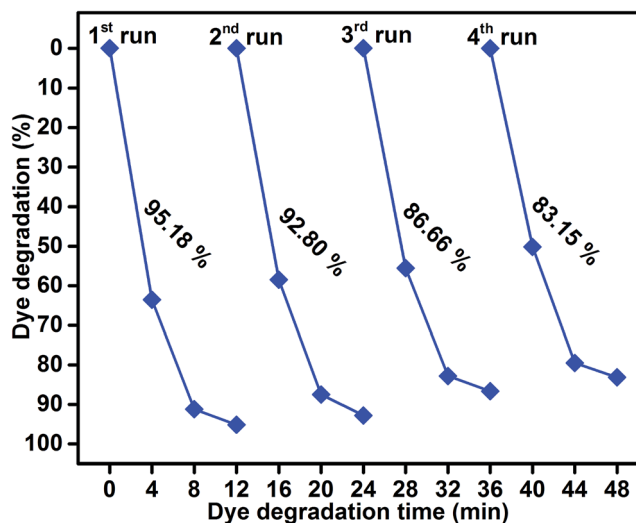


Fig. 9 Reusability of sample S4 photocatalyst under visible-light irradiation.

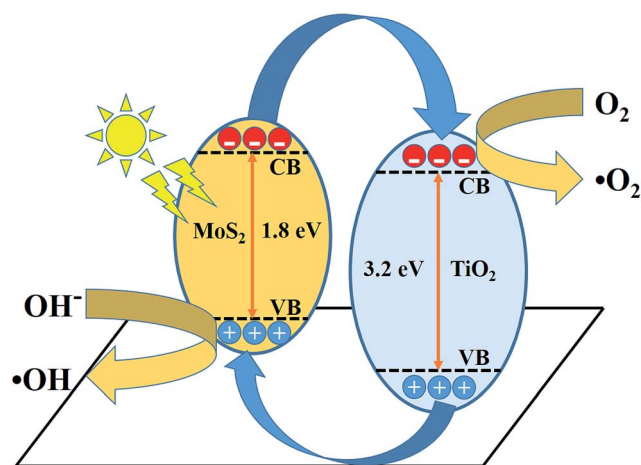


Fig. 10 Schematic of the charge transfer mechanism from MoS₂ to TiO₂ photocatalysis.

4. Conclusion

Pure layered MoS₂ and MoS₂-TiO₂ nanocomposites were successfully synthesized by a facile hydrothermal method. The XRD patterns revealed the hexagonal MoS₂ and anatase structure of TiO₂. The morphological analysis confirmed the presence of layered MoS₂ and TiO₂ nanosheets. The obtained results confirmed that the MoS₂/TiO₂ nanocomposite photocatalyst had enhanced photocatalytic activity for MB degradation under visible-light irradiation. The interfacial charge carriers were transferred between MoS₂ and TiO₂ nanosheets and effectively suppressed the electron hole pair recombination. The maximum degradation efficiency was attained for the MoS₂/TiO₂ (S4) nanocomposite photocatalyst in 12 min. The degradation efficiency obtained for the nanocomposite was three times higher than that obtained for pure MoS₂ and commercial P25 TiO₂. The free radicals trapping experiment confirmed that

photogenerated ([•]OH) radicals played an important role in the degradation of the organic pollutant.

References

- 1 C. Minero, E. Pelizzetti, S. Malato and J. Blanco, *Chemosphere*, 1993, **26**, 2103–2119.
- 2 H. Liu, T. Lv, X. H. Wu and C. K. Zhu, *Appl. Surf. Sci.*, 2014, **30**, 242–246.
- 3 S. Ameen, M. S. Akhtar, M. Nazim and H. S. Shin, *Mater. Lett.*, 2013, **96**, 228–232.
- 4 S. Harish, M. Navaneethan, J. Archana, A. Silambarasan, S. Ponnusamy, C. Muthamizhchelvan and Y. Hayakawa, *Dalton Trans.*, 2015, **44**, 10490–10498.
- 5 A. Fujishima and K. Honda, *Nature*, 1972, **238**, 37–38.
- 6 J. Archana, M. Navaneethan and Y. Hayakawa, *J. Power Sources*, 2013, **242**, 803–810.
- 7 J. Archana, S. Harish, M. Sabarinathan, M. Navaneethan, S. Ponnusamy, C. Muthamizhchelvan, M. Shimomura, H. Ikeda, D. K. Aswal and Y. Hayakawa, *RSC Adv.*, 2016, **6**, 68092–68099.
- 8 B. Banerjee, V. Amoli, A. Maurya, A. Sinha and A. Bhaumik, *Nanoscale*, 2015, **7**, 10504–10512.
- 9 G. H. Moon, W. Kim, D. Bokare, N. Sung and W. Choi, *Energy Environ. Sci.*, 2014, **7**, 4023–4028.
- 10 S. Hernandez, D. Hidalgo, A. Sacco, A. Chiodoni, A. Lamberti, V. Cauda, E. Tresso and G. Saracco, *Phys. Chem. Chem. Phys.*, 2015, **17**, 7775–7786.
- 11 C. Wang, H. Lin, Z. Liu, J. Wu, Z. Xu and C. Zhang, *Part. Part. Syst. Charact.*, 2016, **33**, 221–227.
- 12 H. G. Yang, C. H. Sun, S. Z. Qiao, J. Zou, G. Liu, S. C. Smith, H. M. Cheng and G. Q. Lu, *Nature*, 2008, **453**, 638–641.
- 13 L. Zheng, S. Han, H. Liu, P. Yu and X. Fang, *Small*, 2016, **12**, 1527–1536.
- 14 Y. G. Li, H. L. Wang, L. M. Xie, Y. Y. Liang, G. S. Hong and H. J. Dai, *J. Am. Chem. Soc.*, 2011, **133**, 7296–7299.
- 15 I. Song, C. Park and H. Cheul Choi, *RSC Adv.*, 2015, **5**, 7495–7514.
- 16 T. S. Li and G. L. Galli, *J. Phys. Chem. C*, 2007, **111**, 16192–16196.
- 17 A. Splendiani, L. Sun, Y. Zhang, T. Li, J. Kim, C. Yung, G. Galli and F. Wang, *Nano Lett.*, 2010, **10**, 1271–1275.
- 18 R. Asahi, T. Morikawa, T. Ohwaki, K. Aoki and Y. Taga, *Science*, 2001, **293**, 269–271.
- 19 S. U. M. Khan, M. Al-Shahry and W. B. Ingler, *Science*, 2002, **297**, 2243–2245.
- 20 P. Roy, S. Berger and P. Schmuki, *Angew. Chem., Int. Ed.*, 2011, **50**, 2904–2939.
- 21 J. Schneider, M. Matsuoka, M. Takeuchi, J. Zhang, Y. Horiuchi, M. Anpo and D. W. Bahnemann, *Chem. Rev.*, 2014, **114**, 9919–9986.
- 22 J. R. Chen, F. X. Qiu, W. Z. Xu, S. S. Cao and H. J. Zhu, *Appl. Catal., A*, 2015, **495**, 131–140.
- 23 H. Y. Liu, J. B. Joo, M. Dahl, L. S. Fu, Z. Z. Zeng and Y. D. Yin, *Energy Environ. Sci.*, 2015, **8**, 286–296.
- 24 C. J. Liu, S. Y. Tai, S. W. Chou, Y. C. Yu, K. D. Chang, S. Wang, F. S. Chien, J. Y. Lin and T. W. Lin, *J. Mater. Chem.*, 2012, **22**, 21057–21064.



- 25 K. H. Hu, Y. Xu, E. Z. Hu, J. H. Guo and X. G. Hu, *Tribol. Int.*, 2016, **104**, 131–139.
- 26 Y. Jun Yuan, Z. Jun Ye, H. Wei Lu, B. Hu, Y. Hui Li, D. Qin Chen, J. Song Zhong, Z. Tao Yu and Z. Gang Zou, *ACS Catal.*, 2016, **6**, 532–541.
- 27 H. Li, K. Yu, X. Lei, B. Guo, C. Li, H. Fu and Z. Zhu, *Dalton Trans.*, 2015, **44**, 10438–10447.
- 28 N. Meng, Y. Zhou, W. Nie, L. Song and P. Chen, *J. Nanopart. Res.*, 2015, **17**, 300–310.
- 29 G. Zhou, X. Xu, J. Yu, B. Feng, Y. Zhang, J. Hu and Y. Zhou, *CrystEngComm*, 2014, **16**, 9025–9032.
- 30 Q. Xiang, J. Yu and M. Jaroniec, *J. Am. Chem. Soc.*, 2012, **134**, 6575–6578.
- 31 Y. Gai, J. Li, S. S. Li, J. B. Xia and S. H. Wei, *Phys. Rev. Lett.*, 2009, **102**, 036402–036405.
- 32 Z. B. Chen, D. Cummins, B. N. Reinecke, E. Clark, M. K. Sunkara and T. F. Jaramillo, *Nano Lett.*, 2011, **11**, 4168–4175.
- 33 B. Pourabbas and B. Jamshidi, *Chem. Eng. J.*, 2008, **138**, 55–62.
- 34 X. Zu, C. Yang, F. Xiao, J. Wang and X. Su, *New J. Chem.*, 2015, **39**, 683–688.
- 35 L. Cao, R. Wang, D. Wang, X. Li and H. Jia, *Mater. Lett.*, 2015, **160**, 286–290.
- 36 R. Tang, R. Yin, S. Zhou, T. Ge, Z. Yuan, L. Zhang and L. Yin, *J. Mater. Chem. A*, 2017, **5**, 4962–4971.
- 37 H. Li, Y. Wang, G. Chen, Y. Sang, H. Jiang, J. He, X. Li and H. Liu, *Nanoscale*, 2016, **8**, 6101–6109.
- 38 M. Shen, Z. Yan, L. Yang, P. Du, J. Zhang and B. Xiang, *Chem. Commun.*, 2014, **50**, 15447–15449.
- 39 X. Zong, H. J. Yan, G. P. Wu, G. J. Ma, F. Y. Wen, L. Wang and C. Li, *J. Am. Chem. Soc.*, 2008, **130**, 7176–7177.
- 40 W. Zhou, Z. Yin, Y. Du, X. Huang, Z. Zeng, Z. Fan, H. Liu, J. Wang and H. Zhang, *Small*, 2013, **9**, 140–147.
- 41 H. L. Wang, L. S. Zhang, Z. G. Chen, J. Q. Hu, S. J. Li and Z. H. Wang, *Chem. Soc. Rev.*, 2014, **43**, 5234–5244.
- 42 M. Sabarinathan, S. Harish, J. Archana, M. Navaneethan, H. Ikeda and Y. Hayakawa, *RSC Adv.*, 2016, **6**, 109495–109505.
- 43 S. Harish, J. Archana, M. Navaneethan, A. Silambarasan, K. D. Nisha, S. Ponnusamy, C. Muthamizhchelvan, H. Ikeda, D. K. Aswal and Y. Hayakawa, *RSC Adv.*, 2016, **6**, 89721–89731.
- 44 Y. Yan, B. Xia, N. Li, Z. Xu, A. Fisher and X. Wang, *J. Mater. Chem. A*, 2015, **3**, 131–135.
- 45 F. A. Deorsola, N. Russo, G. A. Blengini and D. Fino, *Chem. Eng. J.*, 2012, **1–6**, 195–196.
- 46 J. Baltrusaitis, C. R. Usher and V. H. Grassian, *Phys. Chem. Chem. Phys.*, 2007, **9**, 3011–3024.
- 47 L. Peitao, L. Yonggang, Y. Weichun, M. Ji and G. Daqiang, *Nanotechnology*, 2016, **27**, 225403–225410.
- 48 G. Gong, Y. Liu, B. Mao, B. Wang, L. Tan, D. Li, Y. Liu and W. Shi, *RSC Adv.*, 2016, **6**, 99023–99033.
- 49 S. Zheng, Y. Cai and K. E. O'Shea, *J. Photochem. Photobiol., A*, 2010, **210**, 61–68.
- 50 P. Zheng, Z. Pan, H. Li, B. Bai and W. Guan, *J. Mater. Sci.: Mater. Electron.*, 2015, **26**, 6399–6410.
- 51 X. V. Doorslaer, P. M. Heynderickx, K. Demeestere, K. Debevere, H. V. Langenhove and J. Dewulf, *Appl. Catal., B*, 2012, **111–112**, 150–156.
- 52 W. Ho, J. C. Yu, J. Lin, J. Yu and P. Li, *Langmuir*, 2004, **20**, 5865–5869.
- 53 Y. Liu, Y. X. Yu and W. D. Zhang, *J. Phys. Chem. C*, 2013, **117**, 12949–12957.
- 54 E. Scalise, M. Houssa, G. Pourtois, V. V. Afanas'ev and A. Stesmans, *Phys. E*, 2014, **56**, 416–421.
- 55 K. Hong Hu, Y. Kui Cai and S. Li, *Adv. Mater. Res.*, 2011, **197–198**, 996–999.
- 56 K. Hong Hu, X. Guo Hu and Y. Fu Xu, *J. Mater. Sci.*, 2010, **45**, 2640–2648.
- 57 W. Zhang, X. Xiao, L. Zheng and C. Wan, *Can. J. Chem. Eng.*, 2015, **93**, 1594–1602.
- 58 D. Yong, Z. Yifeng, N. Wangyan and C. Pengpeng, *Appl. Surf. Sci.*, 2015, **357**, 1606–1612.

